Estimate of the Predictability of Boreal Summer and Winter Intraseasonal Oscillations from Observations

RUIQIANG DING AND JIANPING LI

State Key Laboratory of Numerical Modeling for Atmospheric Sciences and Geophysical Fluid Dynamics (LASG), Institute of Atmospheric Physics, Chinese Academy of Sciences, Beijing, China

KYONG-HWAN SEO

Department of Atmospheric Sciences, Pusan National University, Busan, South Korea

(Manuscript received 30 July 2010, in final form 15 February 2011)

ABSTRACT

Tropical intraseasonal variability (TISV) shows two dominant modes: the boreal winter Madden–Julian oscillation (MJO) and the boreal summer intraseasonal oscillation (BSISO). The two modes differ in intensity, frequency, and movement, thereby presumably indicating different predictabilities. This paper investigates differences in the predictability limits of the BSISO and the boreal winter MJO based on observational data. The results show that the potential predictability limit of the BSISO obtained from bandpass-filtered (30–80 days) outgoing longwave radiation (OLR), 850-hPa winds, and 200-hPa velocity potential is close to 5 weeks, comparable to that of the boreal winter MJO. Despite the similarity between the potential predictability limits of the BSISO and MJO, the spatial distribution of the potential predictability limit of the TISV during summer is very different from that during winter. During summer, the limit is relatively low over regions where the TISV is most active, whereas it is relatively high over the North Pacific, North Atlantic, southern Africa, and South America. The spatial distribution of the limit during winter is approximately the opposite of that during summer. For strong phases of ISO convection, the initial error of the BSISO shows a more rapid growth than that of the MJO. The error growth is rapid when the BSISO and MJO enter the decaying phase (when ISO signals are weak), whereas it is slow when convection anomalies of the BSISO and MJO are located in upstream regions (when ISO signals are strong).

1. Introduction

The intraseasonal oscillation (ISO) is a dominant mode of low-frequency variability in the tropical troposphere (e.g., Madden and Julian 1994). The mode undergoes a distinct seasonal variation, with most active oscillation during the northern winter and spring, and weaker activity during the northern summer (Slingo et al. 1999). The boreal winter ISO, often referred to as the Madden–Julian oscillation (MJO; Madden and Julian 1994), is characterized by eastward-propagating tropical convective anomalies and associated circulation anomalies with time scales of about 30–70 days. In contrast, the boreal summer ISO (BSISO) has a complex structure that shows both eastward and northward propagation (Yasunari 1979; Lawrence and Webster 2002).

Employing the nonlinear local Lyapunov exponent (NLLE) method, Ding et al. (2010) showed that the potential predictability limit of the ISO obtained from bandpass-filtered (30–80 days) outgoing longwave radiation (OLR) and wind fields can exceed 5 weeks, which is well above the 1-week predictability of background noise due to bandpass filtering. In contrast, an investigation of the predictability of the real-time MJO index, as introduced by Wheeler and Hendon (2004), reveals a predictability limit of about 3 weeks. However, given that Ding et al. (2010) used year-round daily data, which tends to be dominated by the stronger boreal winter phase (MJO) of the tropical intraseasonal variability (TISV), their study mainly considers boreal winter MJO cases. The predictability of the northern

Corresponding author address: Dr. Jianping Li, State Key Laboratory of Numerical Modeling for Atmospheric Sciences and Geophysical Fluid Dynamics (LASG), Institute of Atmospheric Physics, Chinese Academy of Sciences, P.O. Box 9804, Beijing 100029, China. E-mail: ljp@lasg.iap.ac.cn

DOI: 10.1175/2011MWR3571.1

summer ISO obtained from observational data remains unknown.

In the present study, the NLLE approach is employed to separately investigate the predictability limits of the boreal summer ISO and the boreal winter MJO, based on observed daily OLR, 850-hPa wind fields, and 200-hPa velocity potential, in order to identify the differences in the predictability of the boreal summer ISO and the boreal winter MJO (for brevity, we hereafter refer to the boreal summer ISO as the BSISO and the boreal winter MJO as the MJO). In addition, the potential predictability limit of the TISV may be different in different tropical regions; therefore, it is interesting to compare the spatial distributions of the potential predictability limit of the TISV during summer and winter. To examine if the predictability of the BSISO and MJO is phase dependent, the predictabilities of the BSISO and MJO for different phases of strong ISO events are also compared.

2. Application of the NLLE approach

a. NLLE of an n-dimensional dynamical system

Consider a general n-dimensional nonlinear dynamical system whose evolution is governed by

$$\frac{d\mathbf{x}}{dt} = \mathbf{F}(\mathbf{x}), \tag{1}$$

where $\mathbf{x} = [x_1(t), x_2(t), \ldots\ldots, x_n(t)]^{\mathrm{T}}$ is the state vector at the time t, the superscript T is the transpose, and $\mathbf{F}$ represents the dynamics. The evolution of a small error $\delta = [\delta_1(t), \delta_2(t), \ldots\ldots, \delta_n(t)]^{\mathrm{T}}$, superimposed on a state $\mathbf{x}$, is governed by the nonlinear equations:

$$\frac{d}{dt}\boldsymbol{\delta} = \mathbf{J}(\mathbf{x})\boldsymbol{\delta} + \mathbf{G}(\mathbf{x}, \boldsymbol{\delta}), \tag{2}$$

where $\mathbf{J}(\mathbf{x})\boldsymbol{\delta}$ are the tangent linear terms, and $\mathbf{G}(\mathbf{x}, \boldsymbol{\delta})$ are the high-order nonlinear terms of the error $\boldsymbol{\delta}$. Because of some difficulties in solving the nonlinear problem, most previous studies (e.g., Lorenz 1965; Eckmann and Ruelle 1985; Yoden and Nomura 1993; Kazantsev 1999; Ziehmann et al. 2000) assumed that the initial perturbations were sufficiently small that their evolution could be approximately governed by the tangent linear model (TLM) of the nonlinear model:

$$\frac{d}{dt}\boldsymbol{\delta} = \mathbf{J}(\mathbf{x})\boldsymbol{\delta}. \tag{3}$$

However, the evolution of the linear error is characterized by continuous exponential growth, which is not applicable to situations in which the initial errors are not very small (Lacarra and Talagrand 1988; Mu 2000; Ding and Li 2007). Therefore, the nonlinear behaviors of error growth should be considered in determining the limit of predictability. Without a linear approximation, the solutions of Eq. (2) can be obtained by numerically integrating it along the reference solution $\mathbf{x}$ from $t = t_0$ to $t_0 + \tau$:

$$\boldsymbol{\delta}_1 = \boldsymbol{\eta}(\mathbf{x}_0, \boldsymbol{\delta}_0, \tau)\boldsymbol{\delta}_0, \tag{4}$$

where $\boldsymbol{\delta}_1 = \boldsymbol{\delta}(t_0 + \tau), \mathbf{x}_0 = \mathbf{x}(t_0), \boldsymbol{\delta}_0 = \boldsymbol{\delta}(t_0)$, and $\boldsymbol{\eta}(\mathbf{x}_0, \boldsymbol{\delta}_0, \tau)$ is the nonlinear propagator. The NLLE is then defined as

$$\lambda(\mathbf{x}_0, \boldsymbol{\delta}_0, \tau) = \frac{1}{\tau}\ln\frac{\|\boldsymbol{\delta}_1\|}{\|\boldsymbol{\delta}_0\|}, \tag{5}$$

where $\lambda(\mathbf{x}_0, \boldsymbol{\delta}_0, \tau)$ depends in general on the initial state $\mathbf{x}_0$ in phase space, the initial error $\boldsymbol{\delta}_0$, and time τ. The NLLE differs from existing local or finite-time Lyapunov exponents defined based on linear error dynamics (Yoden and Nomura 1993; Kazantsev 1999; Ziehmann et al. 2000), which depend solely on the initial state $\mathbf{x}_0$ and time τ, not on the initial error $\boldsymbol{\delta}_0$. The ensemble mean NLLE over the global attractor of the dynamical system is given by

$$\begin{aligned}\overline{\lambda}(\boldsymbol{\delta}_0, \tau) &= \int_{\Omega} \lambda(\mathbf{x}_0, \boldsymbol{\delta}_0, \tau)\, d\mathbf{x} \\ &= \langle \lambda(\mathbf{x}_0, \boldsymbol{\delta}_0, \tau) \rangle_N, \quad (N \to \infty),\end{aligned} \tag{6}$$

where Ω represents the domain of the global attractor of the system and $\langle\ \rangle_N$ denotes the ensemble average of samples of sufficiently large size N ($N \to \infty$). The mean relative growth of initial error (RGIE) can be obtained by

$$\overline{\Phi}(\boldsymbol{\delta}_0, \tau) = \exp[\overline{\lambda}(\boldsymbol{\delta}_0, \tau)\tau]. \tag{7}$$

Using the theorem from Ding and Li (2007), we obtain

$$\overline{\Phi}(\boldsymbol{\delta}_0, \tau) \xrightarrow{p} c(N \to \infty), \tag{8}$$

where $\xrightarrow{p}$ denotes the convergence in probability and c is a constant that depends on the converged probability distribution P of error growth. The constant c can be considered as the theoretical saturation level of $\overline{\Phi}(\boldsymbol{\delta}_0, \tau)$. Once the error growth reaches the saturation level, almost all information on initial states is lost and the prediction becomes meaningless. Using the theoretical saturation level, the limit of dynamical predictability can be

quantitatively determined (Li et al. 2006; Ding and Li 2007; Li and Wang 2008).

b. *Estimating the NLLE from an observational time series*

For systems whose equations of motion are explicitly known, such as the Lorenz system, we can directly calculate the mean NLLE via numerical integration of the system and its error evolution equations (Ding and Li 2007). However, some parameters and external forcing terms in the dynamic equations of atmospheric motion are explicitly unknown, and there exist uncertainties in determining these parameters and external forcing terms. It is possible to estimate the NLLE by making use of the large amounts of observational data available for the atmosphere. In a previous study, we developed an algorithm that yields estimates of the NLLE and its derivatives based on atmospheric observational data (Ding et al. 2008). Over the past few years, the algorithm has been further improved (Li and Ding 2011). The general idea of the algorithm is to find local analogs of the evolution pattern from observational time series. The local analogs are searched for based on the initial information and evolution information at two different time points in the time series. If the initial distance at two different time points is small and if their evolutions are analogous over a very short interval, it is highly likely that the two points were analogous at the initial time. This analog is referred to as a ''local dynamical analog.'' A brief description of the algorithm is given in the appendix.

As noted by Lorenz (1969), a sufficiently long time series is required when using historical analogs to study atmospheric predictability. It is almost impossible to find good natural analogs within current libraries of historical atmospheric data over large regions such as the Northern Hemisphere. However, it should be noted that the local dynamical analog is searched for from the observational time series for a small local region, for which the small number of spatial degrees of freedom makes it possible to find good local analogs within current libraries of historical atmospheric data, which allows an ensemble average (Van den Dool 1994). In the present study, the number of the spatial degrees of freedom that characterizes the BSISO and MJO is reduced to ~2 by extracting their dominant modes. Therefore, current records of observational data (1979–2008) enable us to find good analogs by using the principal components (PCs) of the dominant EOF modes over the tropics, despite the relatively short length of the records (Van den Dool 1994).

One example of the NLLE algorithm from the Lorenz96 40-variable model (a low-order proxy for an atmospheric model; Lorenz 1996) reveals that the algorithm is entirely applicable in estimating the mean error growth from an experimental time series (Li and Ding 2011). The algorithm can also be applied in studies of atmospheric predictability. Based on atmospheric observational data, the NLLE approach has been used to investigate decadal changes in weather predictability (Ding et al. 2008), the temporal–spatial distribution of the predictability of monthly and seasonal means of climate variables (Li and Ding 2008), and the predictability limit of the MJO (Ding et al. 2010). In the present study, we explore the potential predictability limits of the BSISO and MJO based on the NLLE approach.

3. Data and methodology

Daily OLR data from the National Oceanic and Atmospheric Administration (NOAA) are used to represent large-scale tropical convective activity over tropical ocean and land. Continuous OLR records are available from 1 January 1979 to the present; consequently, we use the continuous 1979–2008 time series in the global tropical strip (30°S–30°N). Primary atmospheric circulation data are extracted from the National Centers for Environmental Prediction–National Center for Atmospheric Research (NCEP–NCAR) reanalysis products (Kalnay et al. 1996), which contain a similar record of 850-hPa winds and 200-hPa velocity potential. Both the OLR and 850-hPa winds are combined and analyzed on a 5° latitude–longitude grid. The 200-hPa velocity potential is analyzed alone on a 5° latitude–longitude grid covering the domain from 30°S to 30°N.

To obtain the intraseasonal signal, the seasonal cycle of daily OLR and 850-hPa winds is first removed by subtracting the time mean and the first three harmonics of the annual cycle, leaving the anomaly fields, which are then bandpass filtered to retain periods in the range of 30–80 days. To identify the dominant ISO signal from the extended boreal summer [May–September (MJJAS)] over the tropics (20°S–30°N), an empirical orthogonal function (EOF) analysis is performed of the combined fields of the bandpass-filtered OLR and 850-hPa winds. Similarly, the dominant MJO signal from the extended boreal winter [November–March (NDJFM)] over the tropics (25°S–25°N) is extracted by an EOF analysis of the combined fields of the bandpass-filtered OLR and 850-hPa winds. In computing the EOFs of combined fields, each field was normalized by its global variance (area-averaged variance over the tropics) before input, following Wheeler and Hendon (2004) and Seo et al. (2009). The spatial patterns of the dominant EOF modes provide a good reflection of large-scale variations in tropical convection and associated surface wind fields; the corresponding PCs of the dominant EOF modes

show how the spatial patterns of these modes oscillate over time.

To investigate the predictability of the large-scale divergent circulation at the 200-hPa level associated with the BSISO and MJO, we also perform an EOF analysis of the 200-hPa velocity potential during the extended boreal winter and extended boreal summer, respectively. Before the EOF analysis, annual cycles of the 200-hPa velocity potential field were removed and intraseasonal periods were captured using a 30–80-day Lanczos filter. EOF analysis isolates the spatial structure of the most dominant modes as well as their propagation in time.

The predictability limits of the BSISO and MJO are investigated by applying the NLLE approach to the PC time series of the dominant EOF modes. Similar to Ding et al. (2010), the vector **Z** in the two-dimensional phase space can be defined by the first two PCs:

$$\mathbf{Z}(t) = \{\mathrm{PC1}(t), \mathrm{PC2}(t)\}. \quad (9)$$

The error of the vector **Z** is measured as the absolute error $\sqrt{(\Delta\mathrm{PC1})^2 + (\Delta\mathrm{PC2})^2}$, where ΔPC1 represents the error in the PC1 axis and ΔPC2 represents the error in the PC2 axis. In the two-dimensional phase space, the mean error growth of the vector **Z** with time can be obtained using the NLLE approach. In the algorithm given in the appendix, the time series of a single variable x is replaced by that of the vector **Z**; the error of the variable x is also replaced by the absolute error of the vector **Z**. Similarly, the vector **Z**, consisting of a greater number of PCs (≥3), may be used to estimate the NLLE using the algorithm given in the appendix. Using the PCs that respectively represent the BSISO and MJO, the seasonal differences in the predictability limits of the BSISO and MJO may be investigated.

Wheeler and Hendon (2004) recently developed a new MJO index based on the first two EOFs of the combined fields of near-equatorially averaged (15°S–15°N) 850- and 200-hPa zonal winds, and OLR data. The projection of daily observation data onto such multiple-variable EOFs yields PC time series that are able to strongly discriminate the 30–80-day signal. Hence, the necessity for time filtering is reduced and the resulting PC time series could be calculated in real time. The pair of PC time series that forms the index is referred to as the real-time multivariate MJO series 1 (RMM1) and 2 (RMM2). Although RMM1 and RMM2 describe the evolution of the MJO along the equator, which is independent of season, the off-equatorial structure captured by these indices still exhibits strong seasonality. Therefore, we can further explore the seasonal differences in the predictability of the BSISO and MJO based on RMM indices, which consist of the vector **Z** in Eq. (9). The predictability of the BSISO and MJO, as obtained from unfiltered data, is different from the potential predictability obtained from bandpass-filtered data, as it provides a measure of real-time prediction skill.

To investigate the dependence of the predictability of the BSISO and MJO on different phases, strong ISO events are identified by selecting the dates when either of the two leading PCs exceeding 1.5 standard deviations during the 30-yr period, following Hendon et al. (2000) and Seo et al. (2005). According to the sign of the PCs, the four phases of the ISO are then designated as PC1+, PC2+, PC1−, and PC2− with each succeeding phase leading the preceding phase by about a quarter of a cycle. Null events are defined as the cases where both leading PCs are simultaneously less than 0.5 standard deviations. The predictability is determined in terms of the mean error growth derived using the NLLE approach based on the dates initialized for these five extreme phases.

4. Results

Figures 1 and 2 show the spatial structures of the two leading EOFs of the combined filtered OLR and 850-hPa winds during the extended winter (NDJFM) and extended summer (MJJAS), respectively. According to the criteria proposed by North et al. (1982), the first two EOFs are well separated from the remaining EOFs and contain the meaningful dynamical signal for both the boreal winter and boreal summer. The first two EOFs during both winter and summer generally appear as a pair that together describe the large-scale propagating convective anomalies and associated wind anomalies. Compared with the extended winter, the first two EOFs during the extended summer show markedly different characteristics in terms of off-equatorial structure and propagation, indicating the seasonality of the ISO.

The first two EOFs during the extended winter depict the familiar structure and evolution of the MJO (Figs. 1a,b). In EOF1, enhanced convection is evident over the eastern Indian Ocean and the Maritime Continent, while reduced convection is seen in the central Pacific. Associated westerly wind anomalies exist over the Indian Ocean, and easterlies exist over the Pacific. In EOF2, enhanced convection moves eastward into the western Pacific. As it passes by the Australian landmass, it shifts southward to be most concentrated at about 10°S. At the same time, reduced convection in the Indian Ocean builds as enhanced convection moves out of the region. The eastward movement of 850-hPa wind anomalies is quicker than convection; consequently, enhanced convection in EOF2 is entirely within the westerlies

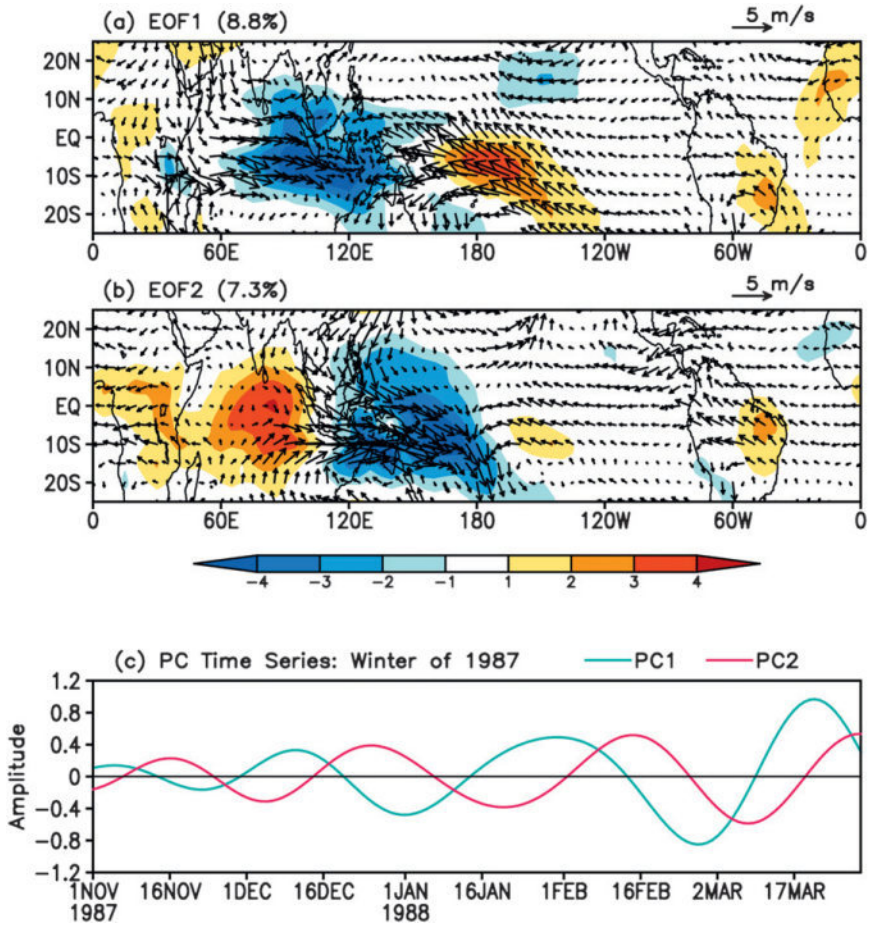

FIG. 1. EOF analysis of the combined fields of 30–80-day-filtered OLR (W m^{-2}) and 850-hPa winds (m s^{-1}) during the extended winter (NDJFM) over the tropics (25°S–25°N). (a) EOF1, (b) EOF2, and (c) PC1 and PC2 from 1 Nov 1987 to 31 Mar 1988.

(over the western Pacific). EOF2 is spatially in quadrature with EOF1. Taken as a pair, these structures are in agreement with the results of previous studies (e.g., Weickmann et al. 1985; Ferranti et al. 1990; Matthews and Kiladis 1999; Innes and Slingo 2003; Wheeler and Hendon 2004) and are effective in capturing the southern summer MJO. The PC time series shows the time-varying amplitude of the EOF spatial structures. A subset of the PC time series (winter of 1987/88) is shown in Fig. 1c. PC1 leads PC2 by about a quarter of a cycle, consistent with the eastward propagation of the MJO.

For the northern summer season, the first two EOFs show eastward and northward propagation of enhanced convection in the Indian Ocean sector (Figs. 2a,b). In EOF1, enhanced convection is present over the eastern equatorial Indian Ocean; in EOF2, it moves northward and eastward into India, the Bay of Bengal, and the Maritime Continent. The associated wind anomalies also show eastward and northward movement, with northeasterly wind anomalies ahead of the enhanced convection (EOF1, EOF2), and southwesterlies behind the convection (EOF2). Because EOF analysis is performed by using information at all longitudes, it is effective in picking up the global signature of the BSISO. In addition to the typical intraseasonal variability of the Indian monsoon, the analysis reveals the variability over the eastern Pacific and Caribbean. All of these aspects of the BSISO that are apparent in the first two EOFs are consistent with those reported in previous studies (Kemball-Cook and Wang 2001; Lawrence and Webster 2002; Wheeler and Hendon 2004), which explored the major characteristics of the BSISO via composite analyses of different phases of the ISO. Figure 2c shows the PC time series of combined fields for the summer of 1987. PC2 leads PC1 by about a quarter of a cycle, describing the eastward- and northward-propagating feature of the BSISO.

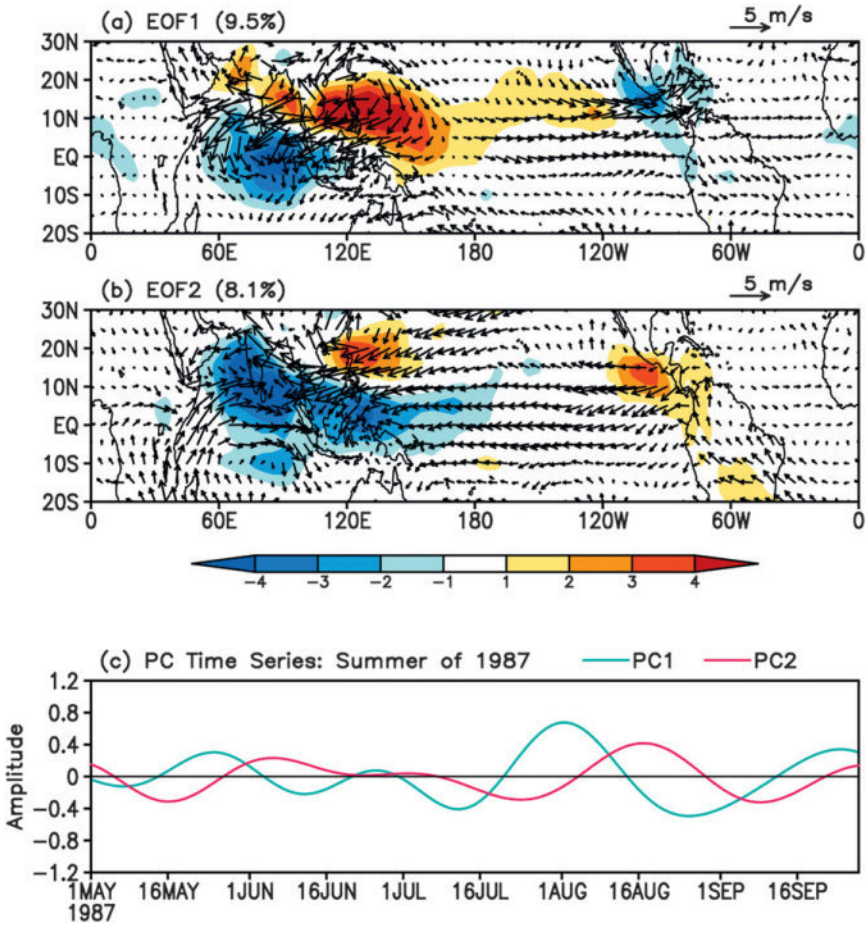

FIG. 2. As in Fig. 1, but for EOF analysis during the extended summer (MJJAS) over the tropics (20°S–30°N). In (c), PC1 and PC2 are shown from 1 May 1987 to 30 Sep 1987.

The above analysis shows that the first two EOFs are able to capture the main characteristics of the BSISO and MJO; consequently, their corresponding PCs may be used to investigate differences in the predictability of the BSISO and MJO. The mean error growth of the vector **Z**, which consists of the first two PCs, can be obtained using the NLLE approach. Figures 3a,b show the mean error growth of the vector **Z** for the BSISO and MJO, respectively. In both cases, the mean error of the vector **Z** shows a rapid initial increase before slowing down and then finally reaching saturation. As noted by Ding et al. (2010), it is possible that mechanisms with different time scales determine the mean error growth of the ISO during different phases of error growth. In the early phase, involving rapid growth of the initial error, the initial conditions may play an important role in determining the mean error growth of the ISO. After about 2 weeks, in contrast, the error growth appears to be more strongly influenced by the slowly varying boundary conditions, such as external SST forcing. Recent observational and modeling studies have shown that ocean–atmosphere coupling is important for maintenance of the ISO, which could lead to an extension of the theoretical predictability of the ISO (Fu et al. 2007; Seo et al. 2007, 2009; Kim et al. 2008). From this viewpoint, ocean–atmosphere coupling could extend the predictability of the ISO to a longer lead time. The mean error growth ultimately reaches the saturation level, indicating that almost all the information on initial states is lost and that the prediction becomes meaningless. Therefore, the potential predictability limit is defined as the time at which the error reaches 95% of its saturation level. From Figs. 3a,b, the potential predictability limits of the BSISO and MJO are about 32 and 34 days, respectively. This result indicates that the potential predictability limit of the MJO is comparable to (but slightly higher than) that of the BSISO.

The potential predictability limits of the BSISO and MJO, as estimated using observational data, are only attained when the models are perfect. Existing models

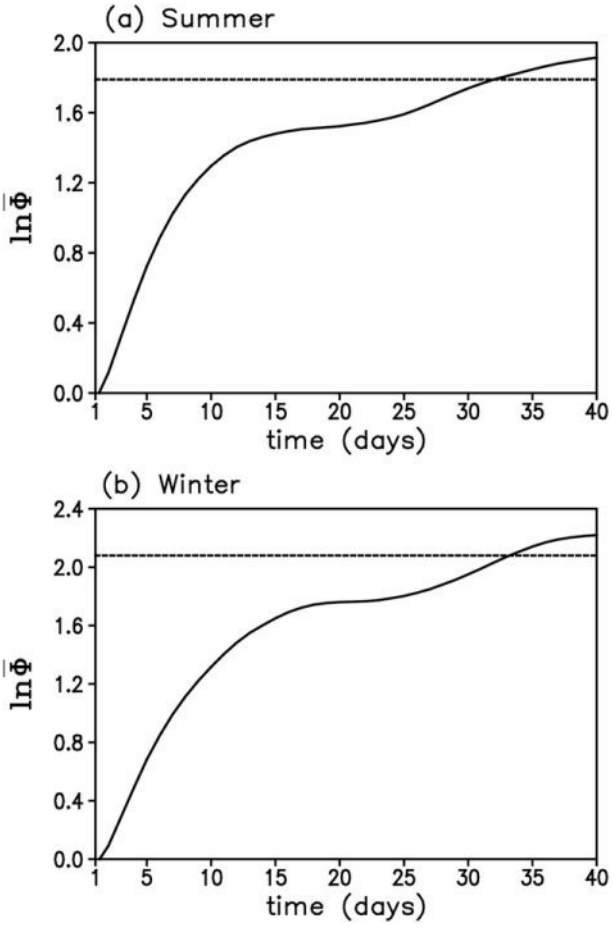

FIG. 3. (a) Mean error growth of the vector **Z** in the two-dimensional phase space defined by the first two PCs of EOF analysis of the combined filtered OLR and 850-hPa winds during the extended summer (MJJAS). (b) As in (a), but for mean error growth of the vector **Z** during the extended winter (NDJFM). The dashed line represents the 95% level of the saturation value, as obtained by taking the average of the mean error growth after 35 days. The $\overline{\Phi}$ denotes the mean error of the vector **Z**.

are commonly poor in simulating the ocean–atmosphere interactions, thereby making it difficult to attain the extended predictability from ocean–atmosphere coupling. The skill of these models is derived mainly from the information contained in the initial states of the atmosphere and ocean. Therefore, most existing models produce low estimates of the prediction skill of the ISO. In Figs. 3a,b, the time taken for the mean error of the vector **Z** to enter the slowly growing phase is around 19 days for the MJO, and around 15 days for the BSISO. These times may represent the predictability of the MJO and the BSISO based mainly on the ISO–MJO signals at the respective initial states. It is evident that during the early phase of error growth, the initial error of the BSISO increases more quickly than that of the MJO. The initially rapid growth of the BSISO error is probably due to its relatively complex spatial structure and propagation pattern (with stronger nonlinearity and instability, which causes initial errors to grow more rapidly). If models with poor representation of the ocean–atmosphere coupling are used to predict the ISO, they generally tend to produce more skillful predictions during winter than during summer.

Figures 4 and 5 show the spatial patterns of the two leading EOFs of 200-hPa velocity potential during the extended boreal winter (NDJFM) and extended boreal summer (MJJAS), respectively. For both seasons, the two leading EOFs account for a large portion of the total variance (around 80%), and are well separated from the remaining EOFs. During the extended boreal winter, enhanced divergence (negative velocity potential anomalies) in EOF1 is located over the eastern Indian Ocean and the Maritime Continent; it moves to the western Pacific in EOF2, with the center occurring south of the equator. Together with the PC time series, these first two EOFs describe a regular eastward propagation of the large-scale divergent circulation associated with intraseasonal convective activity. The first two EOFs during the extended boreal summer show similar spatial patterns to those during the extended boreal winter, with the differences being mainly in the location of the divergence and convergence centers. The eastward propagation of large-scale divergent circulation at 200 hPa is prominent during summer, but the northward propagation over the Asian summer monsoon region is not clear. As in Eq. (1), the vector **Z**, consisting of PC1 and PC2 during summer (winter), represents the BSISO (MJO) activity. Figures 6a,b show the mean error growth of the vector **Z** for the BSISO and MJO, respectively. The predictability limit of the BSISO is the same as that of the MJO, being around 32 days. These limits, determined from 200-hPa velocity potential, are comparable to those determined from combined OLR and 850-hPa winds.

However, previous studies suggest that the predictability of the 200-hPa velocity potential associated with the MJO in numerical models is much longer than that of MJO-related rainfall (Waliser et al. 2003; Reichler and Roads 2005). The relatively high predictability of combined OLR and 850-hPa winds in the present study probably arises because the first two EOFs of combined OLR and 850-hPa winds only capture the large-scale circulation features associated with the BSISO and MJO. In fact, the two PCs of combined OLR and 850-hPa winds are closely related to those of the 200-hPa velocity potential. PC1 and PC2 of combined OLR and 850-hPa winds during winter have correlation coefficients of 0.90 and 0.92 with those of the 200-hPa velocity potential for

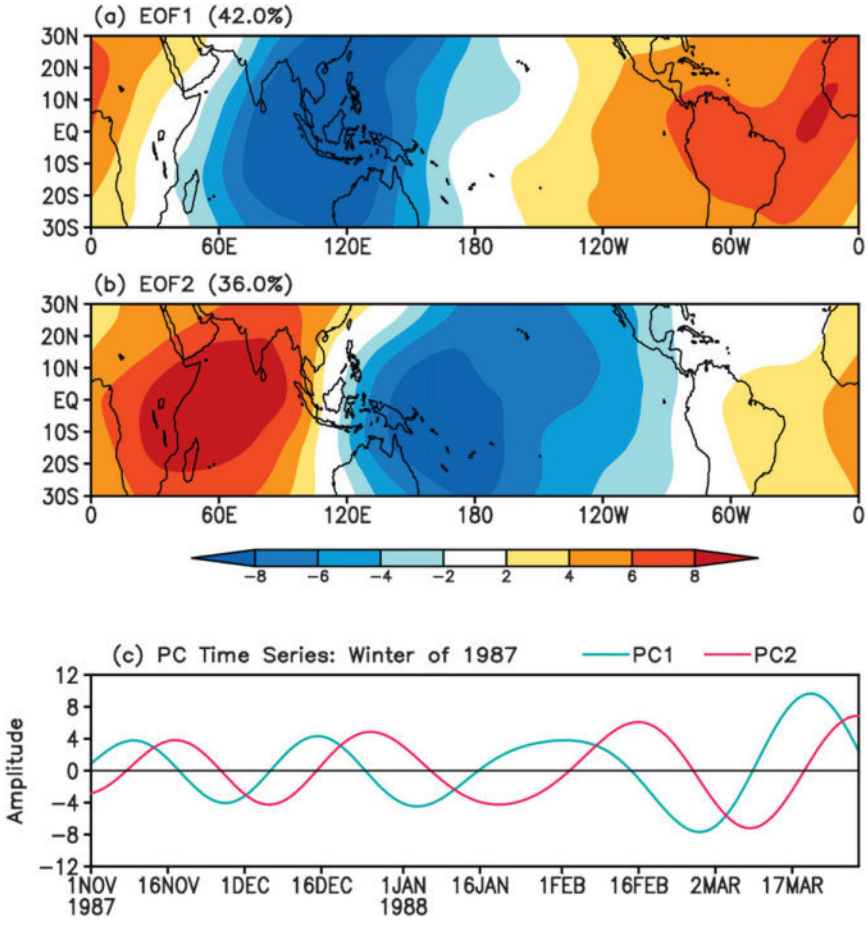

FIG. 4. As in Fig. 1, but for EOF analysis of 30–80-day-filtered 200-hPa velocity potential ($\times 10^5$ m^2 s^{-1}) during the extended winter (NDJFM) over the tropics (30°S–30°N).

1979–2008, respectively. This finding indicates that the first two EOFs of combined OLR and 850-hPa winds are closely coupled with those of the 200-hPa velocity potential, thereby giving a similar predictability of the BSISO and MJO. The total variance explained by the two leading EOFs is relatively small (less than 20%) for combined OLR and 850-hPa winds, suggesting that some BSISO–MJO-related characteristics are not entirely reflected by these two EOFs. EOF3 and EOF4 in the winter MJO show some complicated behavior for combined OLR and 850-hPa winds, with convective activity occurring more to the east of 100°E (Fig. 7). Seo and Kim (2003) reported that EOF1 and EOF2 of the springtime OLR field along the equator clearly show the eastward-propagating OLR variability, while EOF3 shows a stationary convection behavior. Similar to the winter MJO, the spatial patterns of EOF3 and EOF4 in the BSISO are also more complicated than those of EOF1 and EOF2 for combined OLR and 850-hPa winds (Fig. 8). If a greater number of PCs (≥3) are used to calculate the mean error growth of the BSISO and MJO, their predictability would be lower for combined OLR and 850-hPa winds. Figures 9a,b shows the mean error growth of the vector **Z**, which consists of the first three PCs, for the extended summer and extended winter, respectively. In these figures, the predictability limits are around 29 and 30 days for the BSISO and MJO, respectively, lower than the limits shown in Figs. 3a,b. This result indicates that the use of more PCs in the NLLE calculation would reduce the predictability of the BSISO and MJO to some extent for combined OLR and 850-hPa winds. If we measure the predictability of the BSISO–MJO using original filtered data instead of their dominant EOF modes, the predictability of the 200-hPa velocity potential would be higher than that of combined OLR and 850-hPa winds.

As mentioned above, the potential predictability limits obtained by the NLLE approach are close to 5 weeks for the BSISO and MJO, comparable to (but slightly less than) those determined by Ding et al. (2010)

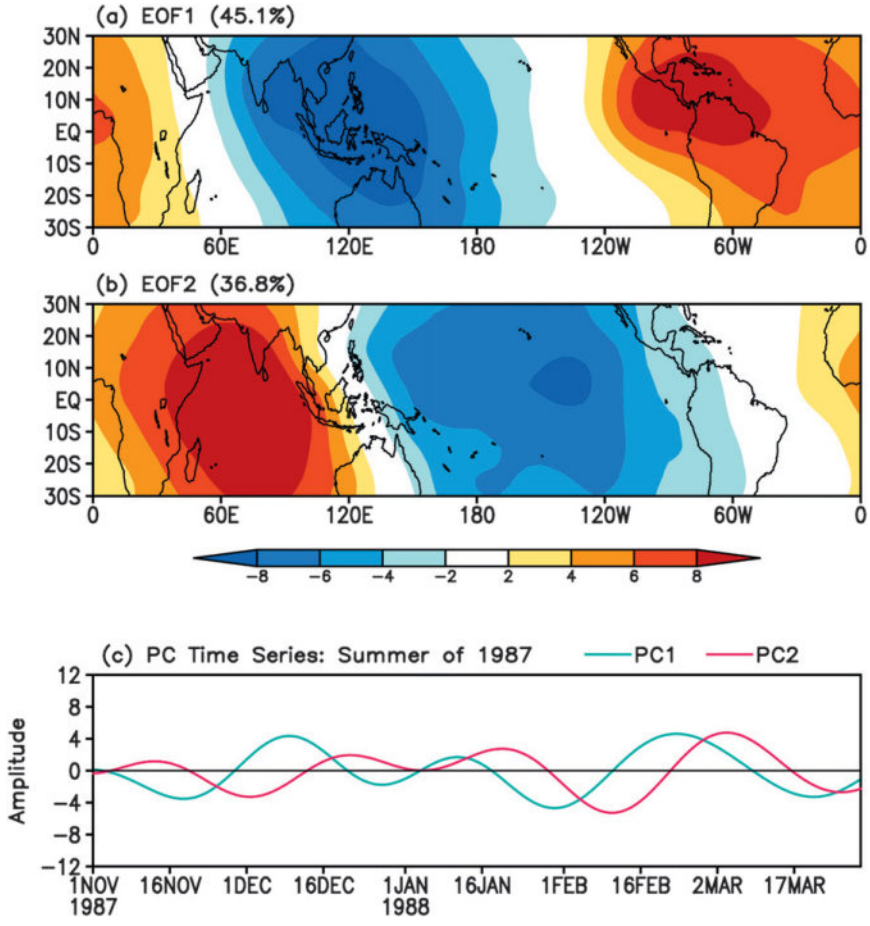

FIG. 5. As in Fig. 2, but for EOF analysis of 30–80-day-filtered 200-hPa velocity potential ($\times 10^5$ m^2 s^{-1}) during the extended summer (MJJAS) over the tropics (30°S–30°N).

from year-round daily data. These results are encouraging, essentially showing that existing numerical and statistical models have great potential to improve the ISO forecasting. However, these potential predictability limits are difficult to attain in real time because they are based on input data with the use of temporal filtering. Temporal filtering has restricted use in real-time predictions because of its requirement for information beyond the end of the time series (Wheeler and Hendon 2004). Moreover, the filtered value for the present day contains information from both past and future days, which tends to inflate the forecast skill as a result of the propagation of observed information into the forecast data (Seo et al. 2009). By generating a set of random numbers with the same spectral characteristics as tropical OLR data, Ding et al. (2010) reported a predictability of about 1 week for background noise arising from bandpass filtering. Here, we perform a similar experiment to test the predictability of filtered noise that has the same spectral characteristics as the two PCs associated with the first two EOFs of combined OLR and 850-hPa winds during the boreal summer and boreal winter, respectively. First, we take the space–time fast Fourier transform (FFT) of the two PCs associated with the BSISO and MJO, multiply them by their conjugate, and then generate random complex numbers that give the same power at each wavenumber and frequency as the PCs. Then, we compute the inverse space–time Fourier transform over the wavenumber-frequency band of the BSISO and MJO to obtain the filtered noise characterized by the same spectrum as the real BSISO and MJO. Finally, we apply the NLLE approach to a time series from the filtered noise and test its predictability. Figures 10a,b shows the probability distributions of the predictability limits of filtered noise with the same spectral characteristics as the BSISO and MJO, respectively. The predictability limits of filtered noise are 5–9 days in both cases, with a maximum probability of 6–7 days, which is much less than 5-week predictability of the BSISO and MJO obtained above. Accordingly, we

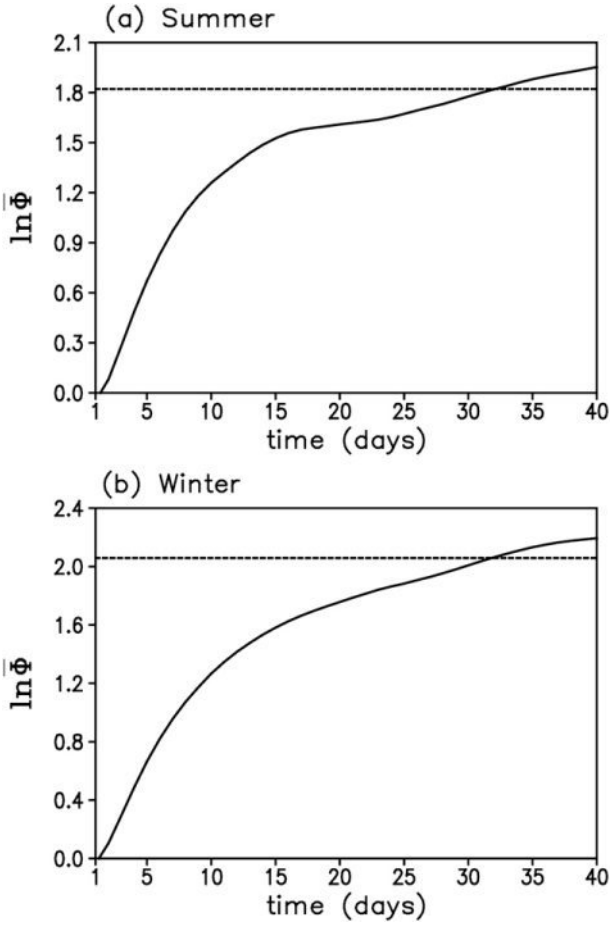

FIG. 6. As in Fig. 3, but for mean error growth of the vector **Z** in the two-dimensional phase space defined by the first two PCs of EOF analysis of the 200-hPa velocity potential during summer and winter.

conclude that the estimated predictability of the BSISO and MJO is not derived from the bandpass filtering itself but from the real signal of the physical processes involved in the development and evolution of the ISO, although the filtering tends to extend the predictability to some extent.

Since the RMM indices, as introduced by Wheeler and Hendon (2004), avoid a bandpass filtering to extract the intraseasonal signals, it is interesting to investigate the predictability limits of the BSISO and MJO using the RMM indices. Figures 11a,b shows the mean error growth of the vector **Z**, which consists of daily RMM1 and RMM2, during the boreal summer and boreal winter, respectively. The predictability limit of the BSISO based on this daily RMM series is around 16 days, while that of the MJO is approximately 18 days. These predictability limits are lower than the potential predictability limit of ~5 weeks obtained above, showing the influence of time filtering on predictability, and thus the smoothness of the evolution of the system. For real-time predictions, the MJO still shows slightly higher predictability than does the BSISO, consistent with the potential predictability obtained from combined OLR and 850-hPa winds. Considering that noise (i.e., signals unrelated to the MJO) is not totally removed from the RMM index and that erratic daily variations remain in the RMM time series (Wheeler and Hendon 2004; Seo et al. 2009; Ding et al. 2010), the predictability limits in real-time predictions of the BSISO and MJO possibly exceed 3 weeks. Figures 12a,b shows the mean error growth of the vector **Z**, which consists of pentad-mean RMM1 and RMM2, during the boreal summer and boreal winter, respectively. The predictability limit of the BSISO based on this pentad RMM series is around 20 days, while that of the MJO is approximately 25 days. The results show that daily weather noise is removed by calculating the pentad mean of daily RMM indices, thereby extending the predictability of the BSISO and MJO.

The above results give a general estimate of the predictability limit of the TISV; however, atmospheric predictability is largely a function of space (González-Miranda 1997; Kumar et al. 2003; Reichler and Roads 2004), indicating that a spatial distribution of the TISV predictability exists in the tropics. The NLLE algorithm allows us to search for local dynamical analogs from observational time series, thereby enabling an estimate of TISV predictability over a small local region or for a single grid point. Based on the NLLE algorithm, the spatial distribution of the predictability limit of the TISV can be determined using combined fields of the bandpass-filtered OLR and 850-hPa winds (each field is normalized by its global variance). Figures 13a,b shows the spatial distributions of the potential predictability limit of the combined filtered (30–80 days) OLR and 850-hPa winds in the tropics (25°S–25°N) during summer and winter, respectively. The potential predictability limit of the TISV ranges from about 28 to 37 days during both summer and winter. The spatial distribution of the limit appears to depend on the season.

During the boreal summer, the potential predictability limit of the TISV is relatively low over the Arabian Sea, India, the Bay of Bengal, the South China Sea, and the western North Pacific, which are the regions where the BSISO is most active. The low predictability of the TISV in these regions is unfavorable to the forecast of the summer TISV. However, the potential predictability limit, which is nearly 1 month, offers a unique opportunity to forecast the summer TISV over an interval that is far beyond the deterministic limit of weather prediction. In contrast, the potential predictability

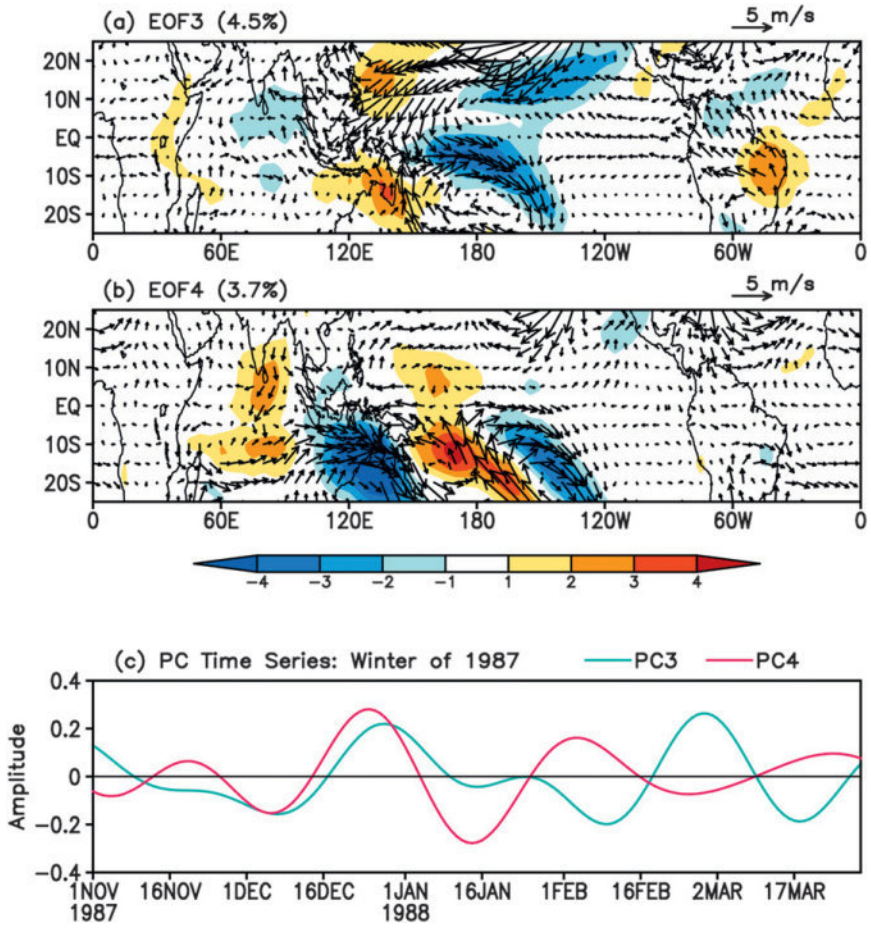

FIG. 7. As in Fig. 1, but for (a) EOF3, (b) EOF4, and (c) PC3 and PC4 from 1 Nov 1987 to 31 Mar 1988.

limit of the summer TISV is relatively high over the North Pacific, North Atlantic, southern Africa, and South America. During the boreal winter, the limit is relatively low over the tropical western Pacific, North Pacific, and North Atlantic, while it is relatively high over the northern Indian Ocean, tropical eastern Pacific, and tropical southern Atlantic. Overall, the spatial distribution of the limit during winter is approximately the opposite of that during summer.

Although the spatial distribution of the potential predictability limit of the TISV is related to that of TISV strength during summer and winter (Figs. 14a,b), the two distributions are not entirely consistent. The summer TISV is relatively strong over the tropical Indian Ocean, the South China Sea, and the northwestern Pacific; in contrast, the winter TISV is relatively strong over the tropical Indian Ocean and northern Australia. The potential predictability limit of the TISV appears to be lower in downstream regions during both seasons (e.g., 10°–20°N region in the Eastern Hemisphere during summer, and 120°E–150°W at the equator during winter). The limit is larger over the onset and development areas of the MJO (including East Africa and the Indian Ocean), where the MJO signal is considerably strong (Fig. 14b). However, this is not the case in summer (Fig. 14a) (probably due to the complex propagation pattern of the BSISO and the weak signal in summer compared with the winter case). The present results indicate that many complex processes and interactions combine to determine the predictability of the TISV, thereby making it difficult to isolate cause-and-effect relationships. Observational data contain the components of both atmospheric internal dynamics and external forcings, and it is difficult to separate these components using current methods. The factors that underlie locally high or low predictability of the summer and winter TISV remain to be identified in future studies using a more realistic model of the TISV.

Figures 15a,b shows the mean error growth of the first two PCs of the combined filtered OLR and 850-hPa

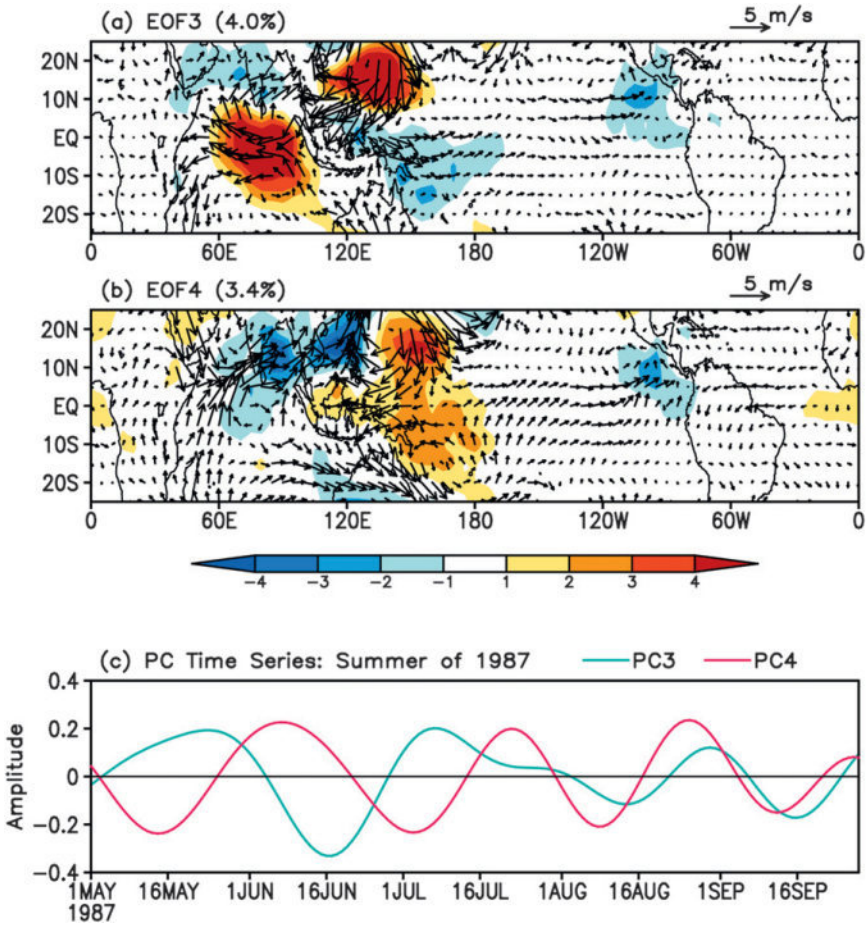

FIG. 8. As in Fig. 2, but for (a) EOF3, (b) EOF4, and (c) PC3 and PC4 from 1 May 1987 to 30 Sep 1987.

winds for the different phases of the life cycle of the BSISO and MJO, respectively. The structures of OLR and 850-hPa winds anomalies for PC1+ and PC2+ initial phases of the BSISO and MJO are shown in Fig. 1 and Fig. 2, respectively. The PC1− and PC2− phases show a structure similar to that of the PC1+ and PC2+, respectively, but with the opposite sign. For both the BSISO and MJO, extreme phases show a lower rate of error growth than the null case. This result is consistent with the findings of Seo et al. (2005), who reported that extreme phases have a skill (measured by the anomaly correlation of upper-level wind) greater than the null case in the NCEP Global Forecast System (GFS) model for both the BSISO and MJO. In general, the initial error of the BSISO shows a rapid initial growth compared with the MJO for cases of strong ISO convection. In contrast, Seo et al. (2005) reported that for cases of strong ISO convection, the forecast skill level of the ISO in the NCEP GFS model is higher during summer than in winter. The prediction skill of the ISO in the NCEP GFS model is only ~7 days (measured by the anomaly correlation), indicating that large deficiencies exist in the NCEP GFS model. Model deficiencies would strongly influence estimates of the prediction skill of the BSISO and MJO. In addition, even if anomaly correlation is a useful measure, it can yield erroneously high scores when the phases of intraseasonal variability are well predicted but the amplitude is poorly predicted. The application of observational data in the present study means that we exclude the influence of model deficiencies, presumably ensuring a more reliable result. We estimated the potential predictability of the BSISO and MJO using indices of combined fields of OLR and 850-hPa winds, whereas Seo et al. (2005) estimated the skill and potential predictability of the BSISO and MJO using zonal winds at 850 and 200 hPa and OLR separately, which may explain the discrepancy between ours results and those of Seo et al. (2005).

Among the four phases of the MJO, the error growth associated with the PC2− is slowest, indicating a smaller

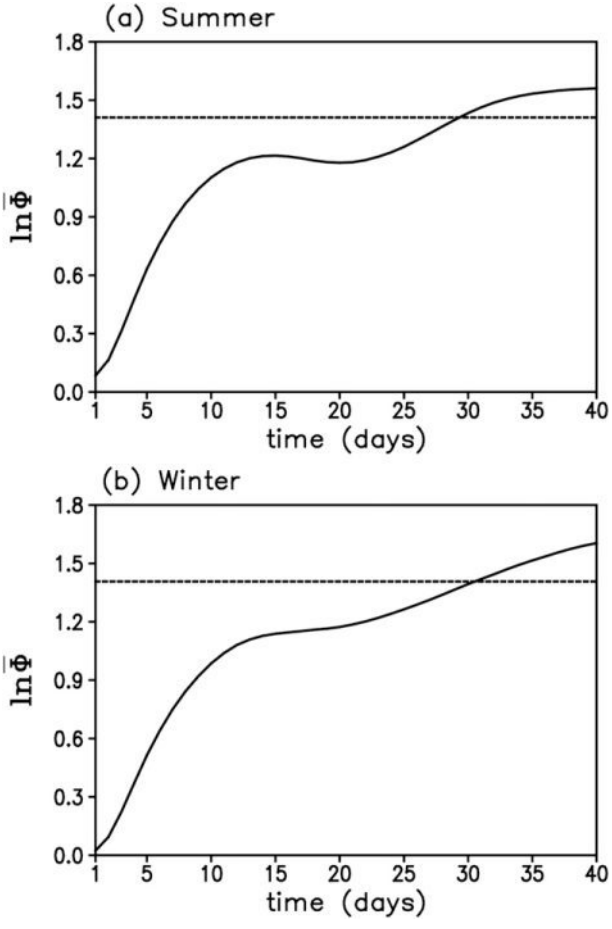

FIG. 9. As in Fig. 3, but for mean error growth of the vector **Z** in the two-dimensional phase space defined by the first three PCs of EOF analysis of combined OLR and 850-hPa winds during summer and winter.

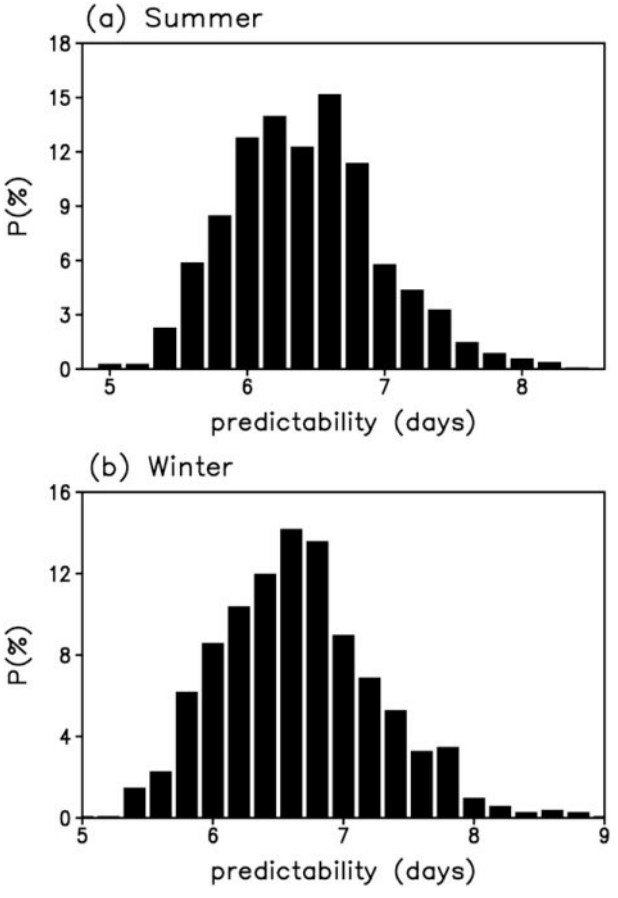

FIG. 10. (a) Probability distribution of the predictability limits based on filtered background noise, which has the same spectral characteristics as two PCs associated with the first two EOFs of combined OLR and 850-hPa winds during the boreal summer. (b) As in (a), but for the boreal winter.

prediction error when MJO convection is initially located over Africa and the Indian Ocean. During the period when the convection anomaly forms over these regions, and subsequently strengthens and moves eastward, it is relatively easy to capture the evolution of the MJO with a small prediction error. The enhanced convection that is initially located over the eastern Indian Ocean and the Maritime Continent (PC1+) also yields a low rate of error growth. Among the four extreme phases of the MJO, the error growth appears to be most rapid during the period when the convection shows a gradual decay in the western Pacific and when the MJO signal is diminishing (PC1−; Fig. 15b). The enhanced convection that is initially located over the western Pacific (PC2+) produces an initial error growth that is slower than that of PC1− but faster than that of PC1+.

Among the four extreme phases of the BSISO, the PC2− phase shows a most rapid growth in initial error, whereas the PC2+ phase shows the slowest growth [Fig. 15a; i.e., the error growth is slow when convection anomalies are initially located over the northern Indian Ocean and the Maritime Continent (PC2+), whereas it is rapid when convection anomalies are initially located over the South China Sea and the western Pacific, and subsequently decay near southern China (PC2−)]. The enhanced convection that is initially located over the eastern Indian Ocean (PC1+) produces an initial error growth similar to or slightly slower than that of PC2−. The error growth is generally rapid when the BSISO and MJO enter the decaying phase (when ISO signals are weak), whereas it is slow when convection anomalies of the BSISO and MJO are located in upstream regions (when ISO signals are strong).

Previous studies have investigated the dependence of ISO predictability on various phases. For example, Waliser et al. (2003) performed a dynamic potential

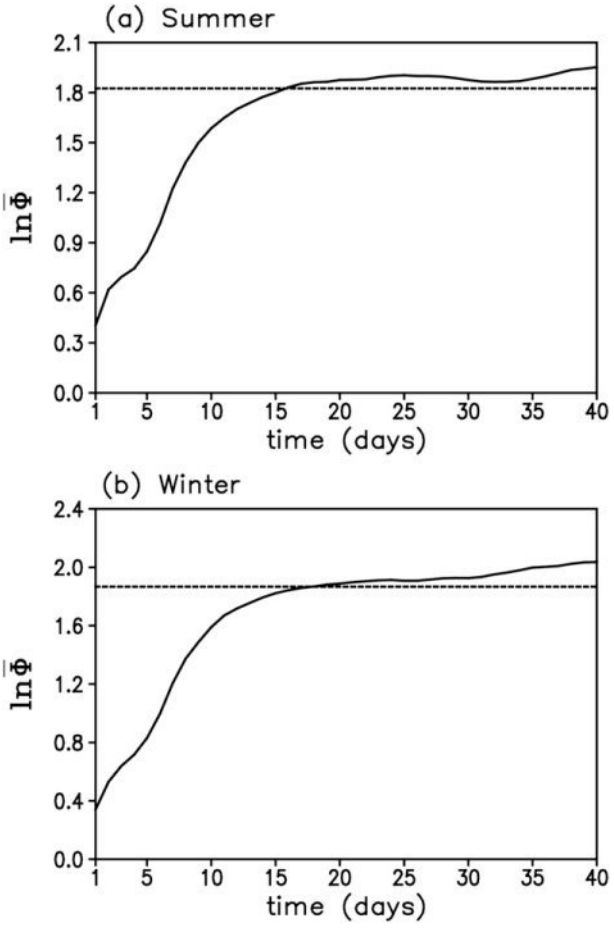

FIG. 11. As in Fig. 3, but for mean error growth of the vector **Z** in the two-dimensional phase space defined by the daily RMM index.

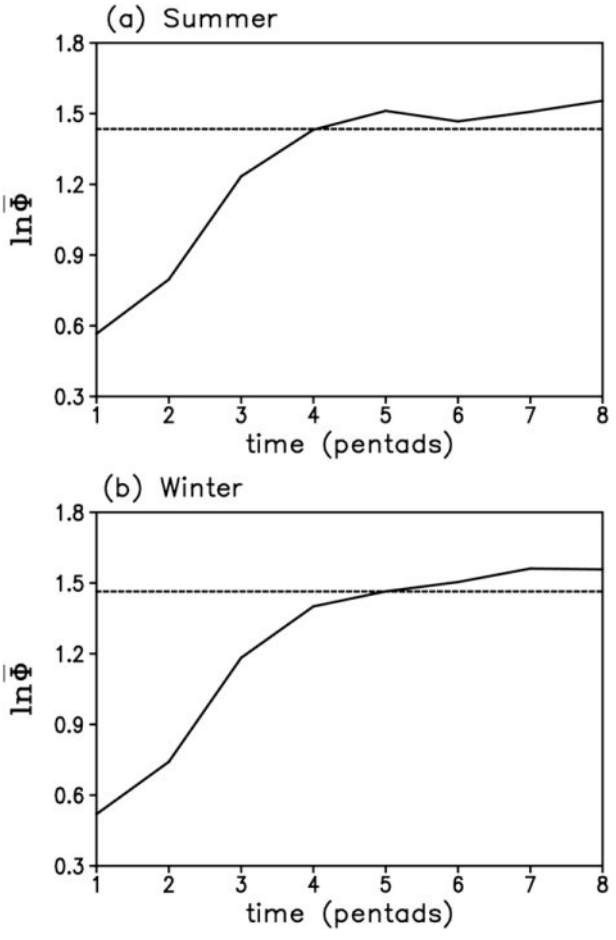

FIG. 12. As in Fig. 11, but for mean error growth of the vector **Z** in the two-dimensional phase space defined by the pentad-mean RMM index.

predictability experiment using the NASA Goddard Laboratory for the Atmospheres (GLA) general circulation model (GCM), and Seo et al. (2005) performed an NCEP GFS forecast experiment. The results of these studies are model dependent, to the extent that different models even yield the opposite conclusions. Some of the present results obtained from observational data are similar to those obtained using models, although other results are dissimilar and some are even contradictory. Further study is necessary to explain the differences between the results obtained from observational data and those obtained from various models.

5. Summary

This study investigated differences in the predictability limits of the BSISO and MJO using the NLLE approach, which provides an estimate of atmospheric predictability based on observational data. The PC time series of the two leading EOFs of the combined filtered OLR and 850-hPa winds during the extended summer (MJJAS) and extended winter (NDJFM) are used as an index of the BSISO and MJO activity, respectively. The potential predictability limit of the BSISO is about 32 days, comparable to (but slightly lower than) that of the MJO (about 34 days). During the early phase of error growth, the initial error of the BSISO grows more rapidly than does that of the MJO, possibly related to the relatively complex spatial variability in BSISO structure. Similar results were found for the filtered 200-hPa velocity potential, revealing that the potential predictability limits of the BSISO and MJO are similar (~32 days). However, the limits estimated using bandpass-filtered data may overestimate the predictability of the ISO because of the use of time filtering. Filtered noise with the same spectral characteristics as the BSISO and MJO shows a predictability of about 1 week. Our investigation of the predictability of the real-time daily MJO index (Wheeler and Hendon 2004) revealed that the upper limits of the

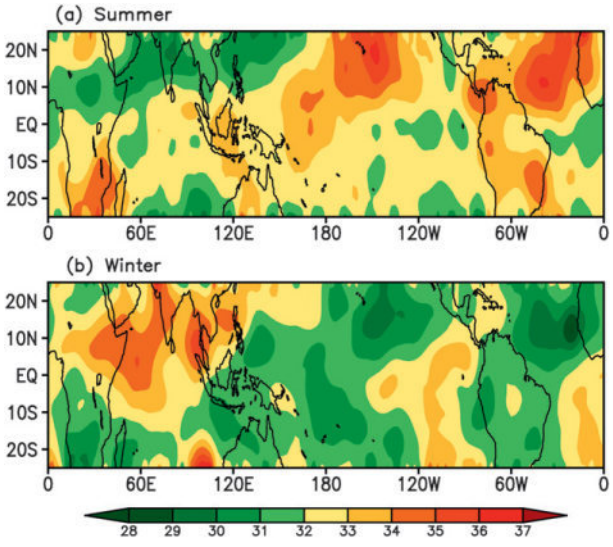

FIG. 13. Spatial distributions of the potential predictability limit of the combined filtered (30–80 days) OLR and 850-hPa winds in the tropics (25°S–25°N) during the (a) extended boreal summer (MJJAS) and (b) extended boreal winter (NDJFM).

forecast skill in real-time predictions of the BSISO and MJO are approximately 16 and 18 days, respectively. The use of pentad-mean RMM indices extends the predictability limit of the BSISO and MJO.

We used the NLLE algorithm to perform a quantitative analysis of the spatial distribution of the potential predictability limit of the combined fields of the bandpass-filtered OLR and 850-hPa winds during summer and winter. Throughout the tropics, the potential predictability limit of the TISV ranges from about 28 to 37 days during both summer and winter. The spatial distribution of the limit appears to depend on the season. During summer, the limit is relatively low over regions where the TISV is most active, whereas it is relatively high over the North Pacific, the North Atlantic, southern Africa, and South America. The spatial distribution of the limit during winter is approximately the opposite of that during summer. For strong phases of ISO convection, the initial error of the BSISO generally shows a more rapid growth than that of the MJO. The error growth is rapid when the BSISO and MJO enter the decaying phase (when ISO signals are weak), whereas it is slow when convection anomalies of the BSISO and MJO are located in upstream regions (when ISO signals are strong).

The present work contains several limitations. First, the total variance explained by the two leading EOFs of combined OLR and 850-hPa winds in the present

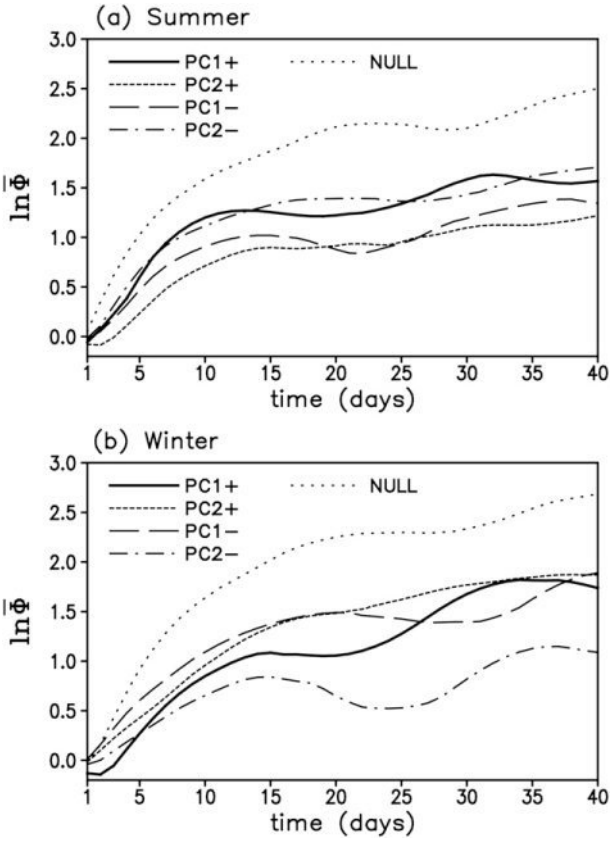

FIG. 15. Mean error growth of the vector **Z** in the two-dimensional phase space defined by the first two PCs of EOF analysis of the combined filtered OLR and 850-hPa winds for the different phases of the (a) BSISO during summer and the (b) MJO during winter.

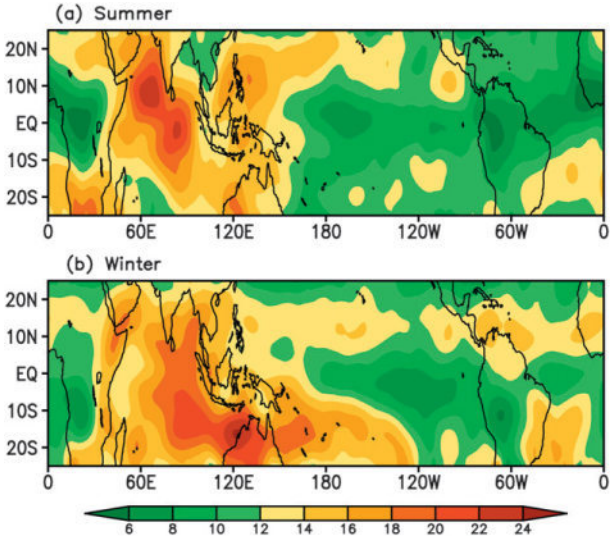

FIG. 14. Percentage of 30–80-day variance to total variance for the (a) extended boreal summer and (b) extended boreal winter OLR field in the tropics (25°S–25°N).

work is relatively small (<20%), which limits the representativeness of the corresponding PC time series used as an index of BSISO and MJO activity. The use of more PCs to calculate the NLLE would be equivalent to increasing the number of spatial degrees of freedom. Clearly, for a relatively short observation period, it is difficult to find good analogs for a large number of spatial degrees of freedom; consequently, the application of the NLLE approach is limited in this situation. Further study is required to assess differences in the predictability of the BSISO and MJO, using a more representative index of ISO activity. Second, the ISO predictability obtained in the present study provides only an estimate of the average predictability of the ISO. Little is known of the physical processes that give rise to the predictability of the BSISO and MJO, which limits our understanding of the BSISO and MJO and hinders their simulation and forecasting. To improve our understanding of the predictability of the TISV, a more realistic model of the ISO is required, as well as a detailed analysis of tropical observational data.

Acknowledgments. We wish to thank Dr. Jiangyu Mao for useful advice and comments. Funding for this research was provided jointly by the 973 program (2010CB950400), NSFC Projects (40805022), and LASG Free Exploration Fund. K.H. Seo was funded by the Korea Meteorological Administration Research and Development Program under Grant CATER 2007-4208.

APPENDIX

An Algorithm for the NLLE Estimation from Observational Data

The experimental or observational data of a single variable of an n-dimensional chaotic system (e.g., the time series of a variable x is given by $\{x(t_i), i = 0, 1, 2, \ldots\ldots, m-1\}$ where m represents the length of the time series), an algorithm that allows the estimation of the mean NLLE and the mean RGIE from the experimental or observational time series is given by the following steps.

Step 1: Taking $x(t_0)$ as the reference point at the time t_0, we first seek the local dynamical analog $x(t_k)$ of the reference point from the dataset. Two distances (i.e., the initial distance between two points and the evolutionary distance between their trajectories within a short initial period) are used to measure the degree of similarity between the points. All points $x(t_j)(|t_j - t_0| > 90$, ensuring that a good analog pair is not merely due to persistence) in the dataset form a set S. The initial distance d_i between the points $x(t_0)$ and $x(t_j)$ is given by

$$d_i = |x(t_0) - x(t_j)|. \tag{A1}$$

We assume that the evolutions of two points are analogous over a very short time τ if they are analogous at the initial time. The choice of the short time interval τ depends on the persistence of the variable x; if the persistence is low, the time over which two initially close points remain analogous is relatively short. The time taken for autocorrelations of the variable x to drop to 0.9 can be regarded as a rough estimate of the short time interval τ. A high value (0.9) of autocorrelation is chosen to ensure a short time interval (the results were found to be insensitive to the selected value). Within the short interval τ ($\tau = K\Delta$, where Δ is the sampling interval of the time series), the evolutionary distance d_e between the two points $x(t_0)$ and $x(t_j)$ is given by

$$d_e = \sqrt{\frac{1}{K+1}\sum_{i=0}^{K}[x(t_i) - x(t_{j+i})]^2}, \tag{A2}$$

where d_i is the amount of the initial separation between the two points $x(t_0)$ and $x(t_j)$, while d_e is the evolutionary distance between their trajectories over a short initial period. The total distance d_t, considering not only the initial distance but also the evolutionary distance, is found by adding d_i and d_e:

$$d_t = d_i + d_e. \tag{A3}$$

If d_t is very small, it is highly likely that the points $x(t_0)$ and $x(t_j)$ are analogous at the initial time. Of course, this approach is unlikely to exclude the possibility that only the variable x remains close, whereas other variables evolve very differently over time, especially for high-dimensional dynamical systems; however, our experimental results indicate that this possibility is low (Li and Ding 2011). For two nonanalogous initial states, the value of d_t is generally large. The constraint of the total distance d_t allows us to exclude a large portion of all points with large initial distances, thereby helping us to find a truly analog of the reference point. For every point $x(t_j)$ in the set S, the value of d_t can be determined. The nearest neighbor (local dynamical analog) $x(t_k)$ of the reference point $x(t_0)$ can be chosen from the set S only if the d_t is the minimum. Then, the initial distance between $x(t_0)$ and $x(t_k)$ is denoted as follows:

$$L(t_0) = |x(t_0) - x(t_k)|. \quad \text{(A4)}$$

Step 2: At the time $t_i = t_0 + i \times \Delta$ $(i = 1, 2, 3, \ldots\ldots)$, $x(t_0)$ will have evolved to $x(t_i)$ along the reference trajectory, and $x(t_k)$ will have evolved into $x(t_{k+i})$. The initial difference $L(t_0)$ will have become

$$L(t_i) = |x(t_i) - x(t_{k+i})|. \quad \text{(A5)}$$

The growth rate of the initial error during the time $t_i - t_0$ is

$$\xi_1(t_i) = \frac{1}{t_i - t_0} \ln \frac{L(t_i)}{L(t_0)}. \quad \text{(A6)}$$

With i gradually increasing, we can obtain the variation of $\xi_1(t_i)$ as a function of the evolution time t_i.

Step 3: Taking $x(t_1)$ as the reference state and repeating the steps 1 and 2 above, we obtain the variation of $\xi_2(t_i)$ as a function of the evolution time t_i.

Step 4: The above procedure is repeated until the reference trajectory has traversed the entire data file. By taking the average of the error growth rates at all reference points, we obtain the mean NLLE:

$$\bar{\xi}(t_i) = \frac{1}{N} \sum_{k=1}^{N} \xi_k(t_i), \quad (i = 1, 2, 3, \ldots\ldots), \quad \text{(A7)}$$

where N $(N < m)$ is the total number of reference points on the reference trajectory.

Step 5: From Eqs. (A6) and (A7), we obtain the approximation of the mean relative growth of initial error (RGIE):

$$\bar{\Phi}(t_i) = \exp[\bar{\xi}(t_i)(t_i - t_0)], \quad (i = 1, 2, 3, \ldots\ldots). \quad \text{(A8)}$$

By investigating the evolution of $\bar{\Phi}(t_i)$ with increasing t_i, we can estimate the mean predictability limit of the variable x.

REFERENCES

Ding, R. Q., and J. P. Li, 2007: Nonlinear finite-time Lyapunov exponent and predictability. *Phys. Lett. A,* **364,** 396–400.

——, ——, and K.-J. Ha, 2008: Trends and interdecadal changes of weather predictability during 1950s–1990s. *J. Geophys. Res.,* **113,** D24112, doi:10.1029/2008JD010404.

——, ——, and K.-H. Seo, 2010: Predictability of the Madden–Julian oscillation estimated using observational data. *Mon. Wea. Rev.,* **138,** 1004–1013.

Eckmann, J. P., and D. Ruelle, 1985: Ergodic theory of chaos and strange attractors. *Rev. Mod. Phys.,* **57,** 617–656.

Ferranti, L., T. N. Palmer, F. Molteni, and K. Klinker, 1990: Tropical–extratropical interaction associated with the 30–60 day oscillation and its impact on medium- and extended-range prediction. *J. Atmos. Sci.,* **47,** 2177–2199.

Fu, X., B. Wang, D. Waliser, and L. Tao, 2007: Impact of atmosphere–ocean coupling on the predictability of monsoon intraseasonal oscillations. *J. Atmos. Sci.,* **64,** 157–174.

González-Miranda, J. M., 1997: Predictability in the Lorenz low-order general atmospheric circulation model. *Phys. Lett. A,* **233,** 347–354.

Hendon, H. H., B. Liebmann, M. Newman, J. D. Glick, and J. E. Schemm, 2000: Medium-range forecast errors associated with active episodes of the Madden–Julian oscillation. *Mon. Wea. Rev.,* **128,** 69–86.

Innes, P. M., and J. M. Slingo, 2003: Simulation of the Madden–Julian oscillation in a coupled general circulation model. Part I: Comparison with observations and an atmosphere-only GCM. *J. Climate,* **16,** 345–364.

Kalnay, E., and Coauthors, 1996: The NCEP/NCAR 40-Year Reanalysis Project. *Bull. Amer. Meteor. Soc.,* **77,** 437–471.

Kazantsev, E., 1999: Local Lyapunov exponents of the quasi–geostrophic ocean dynamics. *Appl. Math. Comput.,* **104,** 217–257.

Kemball-Cook, S., and B. Wang, 2001: Equatorial waves and air–sea interaction in the boreal summer intraseasonal oscillation. *J. Climate,* **14,** 2923–2942.

Kim, H.-M., C. D. Hoyos, P. J. Webster, and I.-S. Kang, 2008: Sensitivity of MJO simulation and predictability to sea surface temperature variability. *J. Climate,* **21,** 5304–5317.

Kumar, A., S. D. Schubert, and M. S. Suarez, 2003: Variability and predictability of 200-mb seasonal mean heights during summer and winter. *J. Geophys. Res.,* **108,** 4169, doi:10.1029/2002JD002728.

Lacarra, J. F., and O. Talagrand, 1988: Short-range evolution of small perturbations in a baratropic model. *Tellus,* **40A,** 81–95.

Lawrence, D. M., and P. J. Webster, 2002: The boreal summer intraseasonal oscillation: Relationship between northward and eastward movement of convection. *J. Atmos. Sci.,* **59,** 1593–1606.

Li, J. P., and R. Q. Ding, 2008: Temporal-spatial distributions of predictability limit of short-term climate (in Chinese with English abstract). *Chin. J. Atmos. Sci.,* **32,** 975–986.

——, and S. Wang, 2008: Some mathematical and numerical issues in geophysical fluid dynamics and climate dynamics. *Commun. Comput. Phys.,* **3,** 759–793.

——, and R. Q. Ding, 2011: Temporal–spatial distribution of atmospheric predictability limit by local dynamical analogs. *Mon. Wea. Rev.,* in press.

——, ——, and B. H. Chen, 2006: Review and prospect on the predictability study of the atmosphere. *Review and Prospects of the Developments of Atmosphere Sciences in Early 21st Century,* China Meteorology Press, 96–104.

Lorenz, E. N., 1965: A study of the predictability of a 28-variable atmospheric model. *Tellus,* **17,** 321–333.

——, 1969: Atmospheric predictability as revealed by naturally occurring analogues. *J. Atmos. Sci.,* **26,** 636–646.

——, 1996: Predictability: A problem partly solved. *Proc. ECMWF Seminar on Predictability*, Vol. I, Reading, United Kingdom, ECMWF, 1–18.

Madden, R. A., and P. R. Julian, 1994: Observations of the 40–50-day tropical oscillation—A review. *Mon. Wea. Rev.,* **122,** 814–837.

Matthews, A. J., and G. N. Kiladis, 1999: The tropical–extratropical interaction between high-frequency transients and the Madden–Julian oscillation. *Mon. Wea. Rev.,* **127,** 661–677.

Mu, M., 2000: Nonlinear singular vectors and nonlinear singular values. *Sci. China,* **43D,** 375–385.

North, G. R., T. L. Bell, R. F. Cahalan, and F. J. Moeng, 1982: Sampling errors in the estimation of empirical orthogonal function. *Mon. Wea. Rev.,* **110,** 699–706.

Reichler, T., and J. O. Roads, 2004: Time–space distribution of long-range atmospheric predictability. *J. Atmos. Sci.,* **61,** 249–263.

——, and ——, 2005: Long-range predictability in the tropics. Part II: 30–60-day variability. *J. Climate,* **18,** 634–650.

Seo, K.-H., and K.-Y. Kim, 2003: Propagation and initiation mechanisms of the Madden-Julian oscillation. *J. Geophys. Res.,* **108,** 4384, doi:10.1029/2002JD002876.

——, J. K. E. Schemm, C. Jones, and S. Moorthi, 2005: Forecast skill of the tropical intraseasonal oscillation in the NCEP GFS dynamical extended range forecasts. *Climate Dyn.,* **25,** 265–284.

——, ——, W. Wang, and A. Kumar, 2007: The boreal summer intraseasonal oscillation simulated in the NCEP Climate Forecast System (CFS): The effect of sea surface temperature. *Mon. Wea. Rev.,* **135,** 1807–1827.

——, W. Wang, J. Gottschalck, Q. Zhang, J. K. E. Schemm, W. R. Higgins, and A. Kumar, 2009: Evaluation of MJO forecast skill from several statistical and dynamical forecast models. *J. Climate,* **22,** 2372–2388.

Slingo, J. M., D. P. Powell, K. R. Sperber, and F. Nortley, 1999: On the predictability of the interannual behaviour of the Madden-Julian oscillation and its relationship with El Niño. *Quart. J. Roy. Meteor. Soc.,* **125,** 583–609.

Van den Dool, H. M., 1994: Searching for analogues, how long must we wait? *Tellus,* **46A,** 314–324.

Waliser, D. E., K. M. Stern, and C. Jones, 2003: Potential predictability of the Madden-Julian oscillation. *Bull. Amer. Meteor. Soc.,* **84,** 33–50.

Weickmann, K. M., G. R. Lussky, and J. E. Kutzbach, 1985: Intraseasonal (30–60 day) fluctuations of outgoing longwave radiation and 250 mb streamfunction during northern winter. *Mon. Wea. Rev.,* **113,** 941–961.

Wheeler, M., and H. H. Hendon, 2004: An all-season real-time multivariate MJO index: Development of an index for monitoring and prediction. *Mon. Wea. Rev.,* **132,** 1917–1932.

Yasunari, T., 1979: Cloudiness fluctuation associated with the Northern Hemisphere summer monsoon. *J. Meteor. Soc. Japan,* **57,** 227–242.

Yoden, S., and M. Nomura, 1993: Finite-time Lyapunov stability analysis and its application to atmospheric predictability. *J. Atmos. Sci.,* **50,** 1531–1543.

Ziehmann, C., L. A. Smith, and J. Kurths, 2000: Localized Lyapunov exponents and the prediction of predictability. *Phys. Lett. A,* **4,** 237–251.